Journal of Sound and Vibration 374 (2016) 172–184

Contents lists available at ScienceDirect

Journal of Sound and Vibration

journal homepage: www.elsevier.com/locate/jsvi

Characterization of acoustic black hole effect using a one-dimensional fully-coupled and wavelet-decomposed semi-analytical model

Liling Tang [a], Li Cheng [a,*], Hongli Ji [a,b], Jinhao Qiu [b]

[a] Department of Mechanical Engineering, The Hong Kong Polytechnic University, Hong Kong
[b] State Key Laboratory of Mechanics and Control of Mechanical Structures, Nanjing University of Aeronautics and Astronautics, Nanjing 210016, PR China

ARTICLE INFO

Article history:
Received 27 August 2015
Received in revised form
26 January 2016
Accepted 23 March 2016
Handling Editor: L. Huang
Available online 7 April 2016

Keywords:
Acoustic black hole
Mexican hat wavelet-decomposed
Flexural vibration
Damping layers

ABSTRACT

Acoustics Black Hole (ABH) effect shows promising features for potential vibration control and energy harvesting applications. The phenomenon occurs in a structure with diminishing thickness which gradually reduces the phase velocity of flexural waves. The coupling between the tailored ABH structure and the damping layer used to compensate for the adverse effect of the unavoidable truncation is critical and has not been well apprehended by the existing models. This paper presents a semi-analytical model to analyze an Euler-Bernoulli beam with embedded ABH feature and its full coupling with the damping layers coated over its surface. By decomposing the transverse displacement field of the beam over the basis of a set of Mexican hat wavelets, the extremalization of the Hamiltonian via Lagrange's equation yields a set of linear equations, which can be solved for structural responses. Highly consistent with the FEM and experimental results, numerical simulations demonstrate that the proposed wavelet-based model is particularly suitable to characterize the ABH-induced drastic wavelength fluctuation phenomenon. The ABH feature as well as the effect of the wedge truncation and that of the damping layers on the vibration response of the beam is analyzed. It is shown that the mass of the damping layers needs particular attention when their thickness is comparable to that of the ABH wedge around the tip area. Due to its modular and energy-based feature, the proposed framework offers a general platform allowing embodiment of other control or energy harvesting elements into the model to guide ABH structural design for various applications.

1. Introduction

Developing highly-damped and light-weighted structures is of great importance for various engineering problems. Traditional methods such as viscoelastic coating for structural damping enhancement usually require covering structural surface over a large area, thus leading to additional weight [1]. The approach using a graded impedance interface for attenuating structural wave reflections at the edges of plates and bar [2] tackles the abovementioned drawback of traditional methods, but is restricted in practical application due to the technical difficulties in creating suitable impedance

* Corresponding author. Tel.: +852 2766 6769; fax: +852 2365 4703.
E-mail address: li.cheng@polyu.edu.hk (L. Cheng).

http://dx.doi.org/10.1016/j.jsv.2016.03.031

interfaces. Mironov [3] first proposed the concept of Acoustics Black Hole (ABH) by reducing structure thickness according to a power-law profile (with power no less than 2) to gradually reduce the local phase velocity of the flexural waves, achieving zero reflection in the ideal scenario thus creating energy concentration at the tip end [3–5]. ABH effect shows appealing features in vibration control because only a very small amount of damping materials is required at the energy focalization region to achieve efficient damping of flexural waves [6–10]. In addition, it also shows potential in sound radiation control [11,12] and energy harvesting due to the high energy concentration within a confined area [13]. Periodic ABH profiles can also be included in structures to further increase the overall performance [10]. In these applications, on one hand, the addition of vibration control or energy harvesting elements may affect the formation of the ideal ABH through their interference with the host structure; on the other hand, topological or system optimizations may be needed to achieve the maximum performance. To this end, a flexible model, which allows the consideration of the full coupling between the host ABH structure and various control or energy-harvesting elements to be embedded, is of paramount importance.

Among existing models describing the ABH effect, the geometrical acoustic approach [14] was first proposed to analyse the flexural wave propagation in tailored wedges and to calculate the reflection coefficients [6,7] on the premise of smoothness assumption of the thickness profile [15]. The wave would never be reflected back if the thickness of wedge was ideally reduced to zero. However, the unavoidable truncations in real fabricated wedges would significantly increase the reflection coefficients, which can be compensated to a certain extent by covering the wedge surfaces with thin damping layers [6,7]. An impedance method which is not limited by the hypothesis of geometrical acoustics has also been proposed by Georgiev et al. for beam structures, which ultimately leads to the reflection matrix by Riccati equation [16,17]. These two types of approaches only consider semi-infinite structures, even only the ABH wedge part in some cases [6,7]. This is obviously different from the practical situation in which structures are finite in size with real boundary, and an ABH profile is usually only part of conventional structures. All these combined, multiple reflections take place between boundaries as well at the intersection between the ABH portion and the rest of the structure, which cannot be apprehended by the existing models. On the other hand, existing approaches consider the effect of a thin damping layer through Ross–Unar–Kerwin (RUK) model [1], which assumes the thickness of the damping layer is much smaller than that of the wedge. In practice, however, the thickness of even an extremely thin damping layer would be comparable to that of the wedge tip, where ABH effect is the largest, which suggests the importance of considering a few practical issues. The first one is the possible increasing importance of the added mass effect, which has been considered in some previous work [7] for a uniform layer. If one wants to further optimize the damping layer through adjusting its location and shape to achieve maximum damping performance, the added mass and stiffness effect of the damping layer needs to be treated in a more versatile manner. Most importantly, the unavoidable full coupling between the damping layer and the power-law profile wedge might need to be considered to better reflect the reality. This issue becomes even more important when other control and energy harvesting elements are added. The geometrical and material characteristics as well as the location of damping layers are shown to greatly affect the performance of damping layers on energy dissipation [17,18]. An optimization on these parameters as well as the thickness variation of the damping layers might be an additional way to achieve the maximum energy dissipation.

In summary, the full coupling between the damping layers and the ABH taper needs to be considered. Meanwhile, the consideration of more realistic structures with finite size and boundary is necessary to guide the design of practical ABH structures. To this end, a simulation model is necessary, which can truthfully characterize the ABH phenomenon while offering the flexibility of considering additional control and energy harvesting elements for further potential applications.

In this paper, we propose a semi-analytical model to analyze an Euler–Bernoulli beam containing a portion with embedded ABH feature and its full coupling with a thin damping layer over its surface. The beam is of finite length with arbitrary boundary conditions. The speed of the flexural waves and the wavelength remain constant in the uniform portion of the beam. When entering into the tapered region, however, the thickness reduction of the beam reduces the wave speed rapidly, along with a much shortened wavelength. This non-uniform and fast-varying nature of the wavelength creates particular challenges to the modeling. To tackle the problem, a wavelet-decomposed formulation is proposed in this paper. This model takes the damping layer as an integral part of the system, thus conserving its full coupling with the host structure. Meanwhile, due to its energy-based and modular nature, it allows easy extension to further include other embedded control or energy harvesting elements for potential applications. Via Lagrange's equation, Mexican hat wavelets are proposed to decompose the displacement field of the system, leading to the theoretical model presented in Section 2. In Section 3, numerical results are compared with FEM for validation. The ABH features, the effects of the truncation, damping layer and full coupling are investigated. Meanwhile, a preliminary analysis on the location and the shape of the damping layers is carried out to illustrate the versatility of the model. The numerical results from present model are further compared with experimental measurements to confirm the accuracy of this model in Section 4. Finally, conclusions are drawn in Section 5.

2. Theoretical model and formulation

2.1. Modeling procedure

As shown in Fig. 1, consider an Euler–Bernoulli beam undergoing flexural vibration under a point force excitation $f(t)$ at x_f. The response is measured at point x_m. The beam is composed of a uniform portion with constant thickness h_b from x_{b1} to

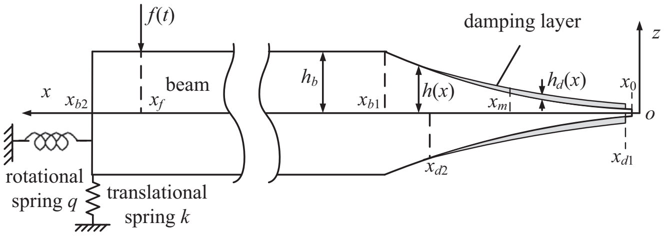

Fig. 1. An Euler–Bernoulli beam with symmetrical ABH power-law profiles.

x_{b2}, an ABH portion with power-law profiled thickness, *i.e.* $h(x)=\varepsilon x^m$, from x_0 and x_{b1}, and damping layers with variable thickness $h_d(x)$ from x_{d1} and x_{d2}. The whole system is assumed symmetrical with respect to the mid-line of the beam. The non-uniform end of the beam is free and the other end is elastically supported by artificial translational and rotational springs [19,20], the stiffness of which can be adjusted to achieve various boundary conditions. For example, if the stiffnesses of the translational and rotational springs are both set to be extremely high compared with that of the beam, a clamped boundary is achieved. This treatment also eliminates the geometrical boundary conditions of the system, thus facilitating the choice of admissible functions in the following displacement-discomposed analysis based on Hamilton principle. The damping of both the beam and the damping layer are taken into account through complex stiffness E, *i.e.*, $E=E\ (1+i\eta)$, where η is the damping loss factor.

Based on Euler–Bernoulli beam theory, the displacement field of the beam writes

$$\{u, w\} = \left\{-z\frac{\partial w}{\partial x}, w(x,t)\right\} \tag{1}$$

where the vector $\{u, w\}$ represents the displacement of a point either on the beam or on the damping layers, along x and z directions, respectively. Note the above assumption assumes a perfect bonding of the damping layer with the host beam to ensure the displacement continuity. The flexural displacement w can be expanded as

$$w(x,t) = \sum_i a_i(t)\varphi_i(x) \tag{2}$$

where $\varphi_i(x)$ are the assumed admissible functions and $a_i(t)$ the complex unknowns to be determined.

Upon constructing the Hamiltonian functional, its extremalization leads to the following Lagrange's equations

$$\frac{d}{dt}\left(\frac{\partial L}{\partial \dot{a}_i(t)}\right) - \frac{\partial L}{\partial a_i(t)} = 0 \tag{3}$$

where the Lagrangian of the system L can be expressed as

$$L = E_k - E_p + W \tag{4}$$

in which E_k represents the kinetic energy of the system; E_p the potential energy and W the work done by the external force. They can be obtained by

$$E_k = \frac{1}{2}\int \rho\left(\frac{\partial w}{\partial t}\right)^2 \mathrm{d}V \tag{5}$$

$$E_p = \frac{1}{2}\int EI(x)\left(\frac{\partial^2 w}{\partial x^2}\right)^2 \mathrm{d}x + \frac{1}{2}kw(x_{b2},t)^2 + \frac{1}{2}q\left(\frac{\partial w(x_{b2},t)}{\partial x}\right)^2 \tag{6}$$

$$W = f(t)\cdot w(x_f, t) \tag{7}$$

Keeping in mind that the kinetic energy and the potential energy in Eqs. (5) and (6) are the sum of the whole system, so the integration should be carried out for both the beam and the damping layers. Based on the energy concept, the damping layers are modeled as part of the system with its intrinsic material properties (modulus E_d, density ρ_d) and full coupling with the beam. Similarly, should other control or energy harvesting elements be present, their energy terms can also be easily added into the system.

Substituting Eqs. (4)–(7) into Eq. (3) yields the following linear equations in matrix form:

$$\mathbf{Ma}(t) + \mathbf{Ka}(t) = \mathbf{f}(t) \tag{8}$$

where $\mathbf{M}$ and $\mathbf{K}$ are, respectively, the mass matrix (real) and stiffness matrix (complex due to the material viscoelasticity); $\mathbf{a}$(t) and $\mathbf{f}$(t) are, respectively, the vector of the response $a_i(t)$ and the force. In a harmonic regime, the vector of the response and the vector of the force are represented as:

$$\mathbf{a}(t) = \mathbf{A}e^{j\omega t} \tag{9}$$

$$\mathbf{f}(t) = \mathbf{F}e^{j\omega t} \tag{10}$$

Then Eq. (8) can be rewritten as,

$$[\mathbf{K} - \omega^2 \mathbf{M}]\mathbf{A} = \mathbf{F} \tag{11}$$

The forced vibration response can be obtained by solving Eq. (11) directly. For free vibration, setting the force vector in Eq. (11) to zero leads to the following eigenvalue equation:

$$\mathbf{M}^{-1}\mathbf{K}\mathbf{A} = \omega^2 \mathbf{A} \tag{12}$$

which gives the natural frequencies and the corresponding mode shapes. Since the system is complex, recalling the express of the stiffness, the eigenvalues take complex form as

$$\omega^2 = \omega_n^2 (1 + i\eta) \tag{13}$$

where ω_n is the natural frequency and η the corresponding modal loss factor of the system. The latter will be particularly useful to characterize the energy absorption of the damping layers as a result of ABH effect.

2.2. Solution using Mexican hat wavelet expansion

In the modelling, the key challenge is to find suitable admissible functions in Eq. (2) to approximate the present displacement field. Although power series (polynomial functions) have been used for non-uniform beams [21,22] or plates [23,24] with linear or nonlinear thickness variation, none of them are comparable to the degree of thickness variation required by ABH profile. In fact, the present non-uniform beam follows power-law profile with thickness quickly diminishing to zero, especially when the power is larger than 2. The resultant rapidly varying wavelength and corresponding increase in vibration amplitude, particularly near the ABH wedge tip, create particular difficulties to the choice of admissible functions. In fact, using polynomial functions to approximate the displacement as a preliminary attempt in our calculation shows strong singularity even with a few expansion terms. The Mexican hat wavelet (MHW) is hereafter demonstrated to be particularly suitable to describe the tightness of the wave packet near the ABH wedge end.

The MHW is the second derivative of the Gaussian distribution function $e^{-\frac{x^2}{2}}$, which can be defined as following after normalization [25,26]

$$\varphi(x) = \frac{2}{\sqrt{3}} \pi^{-\frac{1}{4}} \left[1 - x^2\right] e^{-\frac{x^2}{2}} \tag{14}$$

MHW drops exponentially to zero along x, which can be treated as approximately localized in $[-5, 5]$. After the wavelet transform, the mother wavelet of MHW in Eq. (14) can be expanded into a set of MHW functions

$$\varphi_{j,k}(x) = \frac{2}{\sqrt{3}} \pi^{-\frac{1}{4}} 2^{j/2} \left[1 - (2^j x - k)^2\right] e^{-\frac{(2^j x - k)^2}{2}} \tag{15}$$

where j is the scaling parameter (integer) to stretch or squeeze the MHW and k the translation parameter (integer) to move the MHW along x axis. MHW functions with the scaling parameter $j=0$ and different translation parameters k are shown in Fig. 2. It shows that MHW is highly localized and fairly flexible by scaling and translation, which enables MHW to better cope with the local details of the ABH part. Moreover, the smoothness of MHW is also particularly desirable in the approximation. The abovementioned properties make MHW suitable as the basis functions demonstrated in the latter sections.

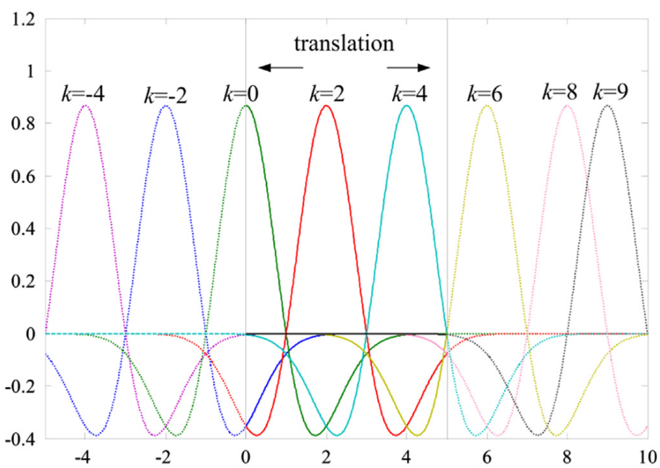

Fig. 2. MHW functions with the scaling parameter $j=0$ and different translation parameters k.

Choosing MHW as basis function, Eqs. (2) and (3) can then be represented as

$$w(x,t)=\sum_{j=0}^{m}\sum_{k}a_{j,k}(t)\varphi_{j,k}(x) \tag{16}$$

$$\frac{\mathrm{d}}{\mathrm{d}t}\left(\frac{\partial L}{\partial \dot{a}_{j,k}(t)}\right)-\frac{\partial L}{\partial a_{j,k}(t)}=0 \tag{17}$$

Another key issue is to choose the appropriate range of translation parameter k when the scaling parameter j is defined. Note that all MHW functions in the beam domain $[x_0, x_{b2}]$ should be included into the displacement expansion in Eq. (16). Meanwhile, to avoid possible singularity of the matrix $\mathbf{K}$ and $\mathbf{M}$, those MHW functions resulting in zero $\int_{x_0}^{x_{b2}}\varphi_{j,k}(x)dx$ value should be eliminated. When calculating $\int_{x_0}^{x_{b2}}\varphi_{j,k}(x)dx$, recall that MHW is treated as approximately localized in $[-5, 5]$. In addition, to avoid possible illness of these matrices, the translation parameter k is determined within the following range:

$$k=[-4+m-j+p(x_0 2^j),\quad g(x_{b2}2^j)+4-m+j],\quad (j=0,1,2,...,m,\quad m\le 5) \tag{18}$$

where $p(*)$ rounds the elements of * to the nearest integers towards zero; $g(*)$ rounds the elements of * to the nearest integers towards infinity. As shown in Fig. 2, setting $x_0=0$, $x_{b2}=5$ cm, $m=0$, and $j=0$, k should be within the range $[-4, 9]$ to ensure that all MHW functions in the beam domain [0, 5] are included. Meanwhile each MHW function with translation k would not result in zero $\int_{x_0}^{x_{b2}}\varphi_{j,k}(x)dx$ value (namely the value of MHW function (solid line) in [0, 5] should not always equal to zero). Eq. (18) shows that under the same scaling parameter j, the range of translation parameter k is larger with the increasing beam length, *i.e.* (x_{b2}–x_0). For a given beam length, however, both j and k can be adjusted to ensure that sufficient terms be used in the expansion to guaranty the calculation accuracy. Expressions to calculate various terms in Eq. (11) by using MHW functions are given in Appendix A.

3. Numerical results and discussion

As a numerical example, the geometrical and material parameters of the beam and the damping layers are shown in Table 1. The beam is clamped-free. A harmonic driving force of 1 N is applied at $x_f=8$ cm. The first resonant frequency of a clamped-free uniform beam with a length of 10 cm and the same material properties is used as the reference frequency [27],

$$f_{\mathrm{ref}}=(\beta l)^2\sqrt{\frac{E_b I}{\rho_b A l^4}}=209.5\ \mathrm{Hz},\quad (\beta l=1.875104) \tag{19}$$

3.1. Validation

We first verify the accuracy of the proposed model when the ABH beam portion is perfectly fabricated without truncation, namely $x_0=0$. Table 2 shows the comparison of first seven resonant frequencies between the FEM results and the results using the present approach. It can be seen that reasonable accuracy is obtained for the lower-order modes up to the fifth or sixth one. The mode shapes trend is also found to be in accordance with that from the FEM results (not shown here). However, when the thickness of the beam tends to zero, the local phase velocity of the flexural waves also approaches to zero and the vibration amplitude becomes infinite theoretically, which can be hardly simulated by either FEM or the present numerical calculation. Therefore, the resonant frequencies and mode shapes cannot exactly match with each other when no truncation exists.

The accuracy of the present approach increases significantly with the appearance of a truncation, even very small. As shown in Table 3 and Fig. 3, the present approach guarantees extremely high accuracy for the first thirty-seven modes in terms of both resonant frequencies (with an error less than 0.5 percent as compared with FEM) and mode shapes when a small truncation ($x_0=1$ cm corresponding to a thickness of the wedge tip of 0.01 cm) is introduced. Fig. 3 shows that ABH

Table 1
Geometrical and material parameters used in the numerical simulation.

Geometrical parameters	Material parameters
	Beam
$\varepsilon=0.005$	$E_b=210$ GPa
$m=2$	$\rho_b=7800$ kg/m^3
$h_b=0.125$ cm	$\eta_b=0.005$
	Damping layers
$x_0=1$ cm	$E_d=5$ GPa
$x_{b1}=5$ cm	$\rho_d=950$ kg/m^3
$x_{b2}=10$ cm	$\eta_d=0.3$

Table 2
Resonant frequency comparison between FEM and present approach results for the beam without truncation $x_0 = 0$.

Resonant frequency (Hz)	FEM	Present approach	Error (%)
ω_1	427.74	427.82	0.017
ω_2	964.47	960.28	−0.434
ω_3	1162.64	1154.94	−0.662
ω_4	1465.12	1470.33	0.355
ω_5	1851.49	1896.61	2.437
ω_6	2306.23	2423.38	5.080
ω_7	2831.84	3071.44	8.461

Table 3
Resonant frequency comparison between FEM and present approach for the beam with truncation $x_0 = 1$ cm.

Resonant frequency (Hz)	FEM	Present approach	Error (%)
ω_1	432.91	432.77	−0.033
ω_2	1669.52	1669.44	−0.005
ω_3	2972.79	2972.68	−0.004
ω_4	5071.01	5071.64	0.012
ω_5	8000.11	8000.41	0.004
ω_6	11338.33	11,338.29	0.000
ω_7	15564.66	15,563.33	−0.009
ω_8	20445.83	20,445.20	−0.003
…	…	…	…
ω_{20}	132394.69	132,388.11	−0.005
ω_{21}	146265.88	146,258.45	−0.005
…	…	…	…
ω_{33}	365983.72	367,427.36	0.394
ω_{34}	388845.60	390,636.11	0.460
ω_{35}	412250.75	413,190.71	0.228
ω_{36}	436519.49	436,889.19	0.085
ω_{37}	461370.85	463,679.23	0.500
ω_{38}	486902.30	493,317.59	1.318
ω_{39}	513248.96	523,609.75	2.019
ω_{40}	540113.58	546,477.55	1.178

takes more significant effect at higher resonant frequencies and the wavelength decreases proportionally to the local phase velocity of the flexural waves in the ABH wedge. Generally speaking, the above results demonstrate that the proposed model together with the use of MHW decomposition can effectively characterize the wavelength fluctuation along the beam as a result of ABH effect and guarantee high accuracy. In addition, treating MHW as approximately localized within a specified region $[-5, 5]$ is also reasonable and will not cause sensible errors in the calculations.

3.2. ABH feature and effects of the truncation and damping layers

Numerical examples are given in the following sections to demonstrate the validity of the model in producing typical ABH phenomenon and its flexibility and versatility to handle various system configurations.

To show the ABH feature and the effect of the truncation on the response, Fig. 4(a) first presents the cross point mobility, $w(x_m = 6\ \text{cm})/f(x_f)$, for ABH beam with or without truncation. The case of a uniform beam with the same length as the ABH beam without truncation is used as reference. It can be seen that the response of the beam with ABH feature is slightly reduced at high frequencies. To further show the overall vibration level, Fig. 4(b) and (c) show the mean quadratic velocity of the uniform portion and the energy ratio Γ between the ABH portion and the uniform portion, respectively. The energy ratio is defined as $\Gamma = 10 \log \frac{<V^2>_{\text{ABH}}}{<V^2>_{\text{Unif}}}$, while the energy ratio of the uniform beam is calculated within the same region corresponding to the ABH beam without truncation. As a result of ABH effect, the vibration level of the uniform portion of the ABH beam is slightly reduced at high frequencies (Fig. 4(b)), in agreement with the cross point mobility curves, and the vibration energy shifts to the ABH part as shown in Fig. 4(c). Not surprisingly, the appearance of the truncation reduces this energy shift thus weakening the ABH effect.

Damping layers are suggested to compensate for the adverse effect induced by the truncation [6,7]. Fig. 5 shows the sufficient increase of the system damping loss factors when damping layers with relatively thin thickness $h_d = 0.005$ cm are applied over the whole surface of the ABH part of the beam. As a reference, the damping layers with same thickness and length are also applied over a uniform beam. Because of the ABH effect at higher frequencies, the concentrating energy on the ABH part enables the damping layers to take much better effect compared with that of the uniform beam, and thus greatly increase the system damping loss factors by as large as 100 percent.

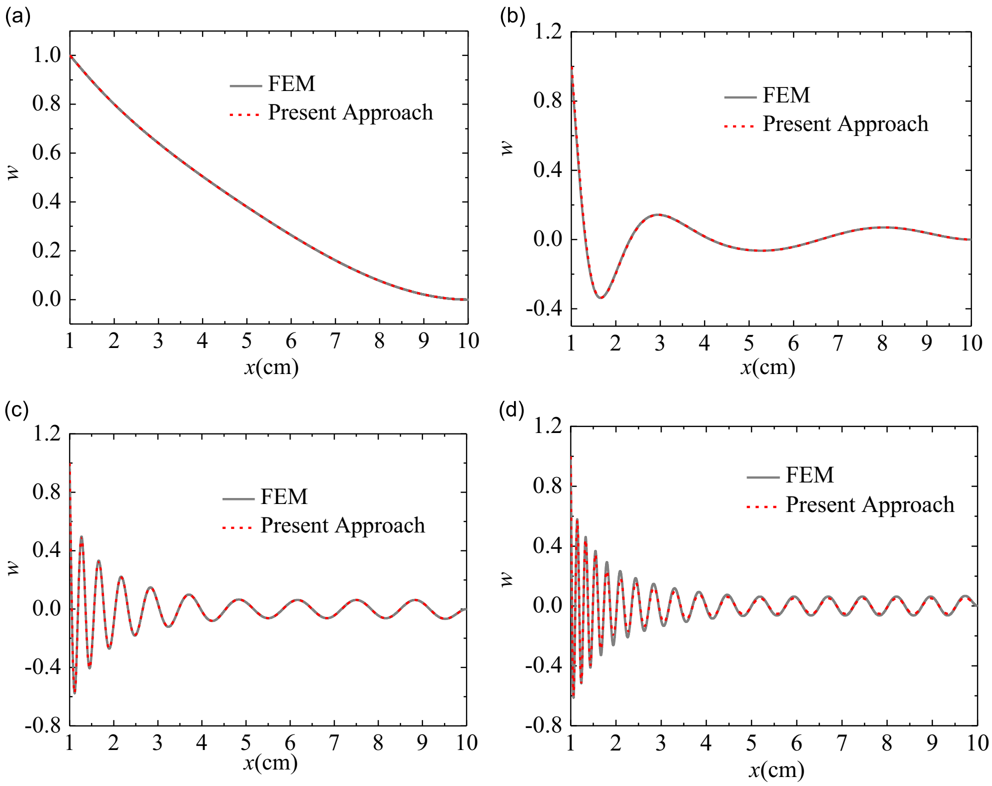

Fig. 3. Mode shape comparison between FEM and present approach when $x_0 = 1$ cm for (a) first mode; (b) fifth mode; (c) twentieth mode; and (d) thirty-fifth mode.

Fig. 6 compares the system damping loss factors η when damping layers with different thicknesses are used to cover the whole surface of the ABH part. At the first resonant frequency where the ABH part does not dominate the vibration mode, the damping layers show little effect on the system damping loss factor. With the increasing input frequency, the ABH part starts to dominate the vibration mode; therefore, thicker damping layers create larger system damping as expected. Typically, the system damping loss factor with damping layers of thickness $h_d = 0.01$ cm (double of the thickness of the ABH tip) is nearly twice as large as that without damping layers ($h_d = 0$). The vibration level of the uniform part and energy ratio are also shown in Fig. 7. Consistent with Fig. 6, the damping layers with thicker thickness reduce the mean quadratic velocity of the uniform part, the maximum of which can be reduced as much as 11.3 dB at the seventh resonant frequency. The damping layers, on the other hand, increase the energy in the ABH part especially at high frequencies as evidenced by an increase in the energy ratio Γ, which demonstrates the compensation effect induced by the surface damping layers.

3.3. Location and thickness variation of damping layers

As demonstrated above, damping layers are effective to increase the system damping at high frequencies and thus compensate to a certain extent the adverse effect of the inevitable truncation. To obtain the maximum damping, the distribution of the damping layers could be adjusted. As an example, the system damping loss factors for different distributions of damping layers with constant mass are compared in Fig. 8. It can be seen that applying damping layers near the ABH tip rather than the whole ABH part significantly increases the system damping loss factor at high frequencies. The maximum loss factor is obtained when the damping layers with thickness of $h_d = 0.01$ cm are deployed in the area from 1 cm to 2 cm, which is close to the ABH tip. Since this small area corresponds to the highest energy density, unit mass of damping layers can consume largest energy and increase the system damping loss factor to maximum content.

Fig. 9 further reveals the effect of the thickness variation of damping layers with constant mass on the system damping loss factor. The damping treatment is applied in the area from 1 cm to 2 cm to gain the maximum damping effect as suggested in Fig. 8. The case with uniform damping layer thickness of $h_d = 0.005$ cm is used as reference. It can be seen that the effect of the shape of the damping layer is not quite obvious for lower-order modes. However, with the increasing ABH effect at higher frequencies, the shape of the damping layer starts to play an important role in determining the overall damping of the system. Roughly speaking, the wave packets shift closer and tighter near the ABH tip with higher energy density when frequency increases as shown in Fig. 3. Therefore, the optimal damping application area also tends to shift towards the ABH tip. Generally, the proposed model provides a tool to eventually optimize the thickness and distribution of

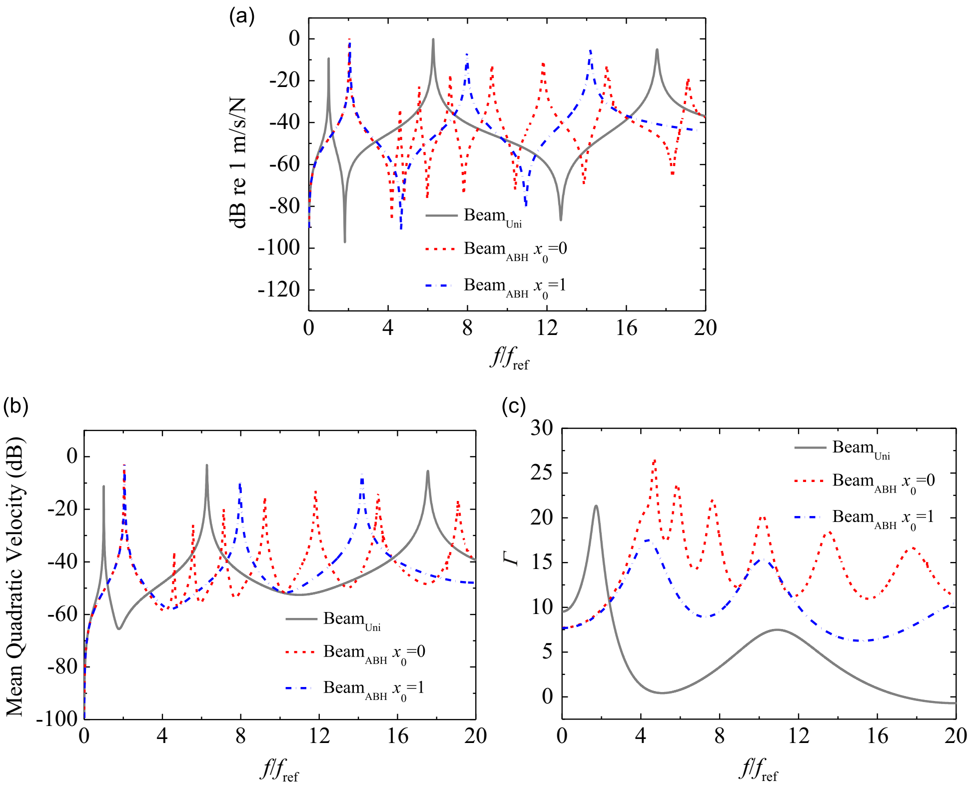

Fig. 4. Comparison of (a) the cross point mobility, $w(x_m=6\ \mathrm{cm})/f(x_f)$, (b) the mean quadratic velocity of the uniform beam portion, and (c) the ratio of mean quadratic velocity of the ABH portion to the uniform beam portion for three different beam conditions.

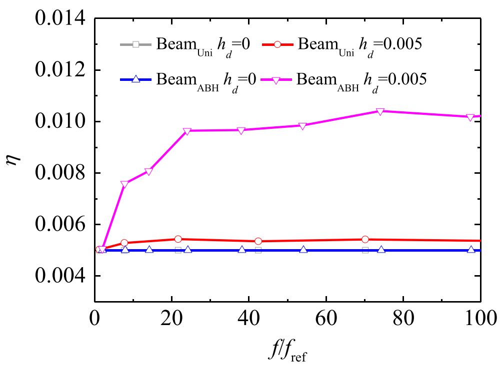

Fig. 5. Effect of damping layers on the system damping loss factors of the uniform beam and the beam with ABH feature, respectively (x_d=1–5 cm).

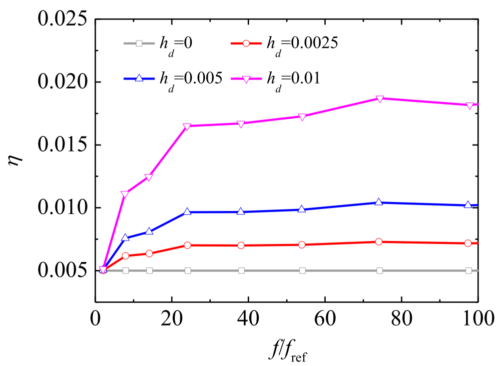

Fig. 6. Comparison of the system damping loss factors for different thicknesses of damping layers when x_d=1–5 cm.

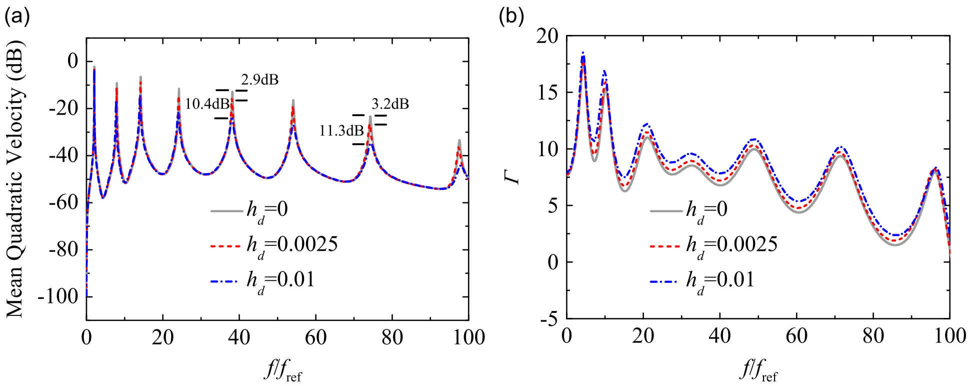

Fig. 7. Comparison of (a) the mean quadratic velocity of the uniform beam portion, and (b) the ratio of mean quadratic velocity of the ABH portion to the uniform beam portion for different thicknesses of damping layers when $x_d = 1$–5 cm.

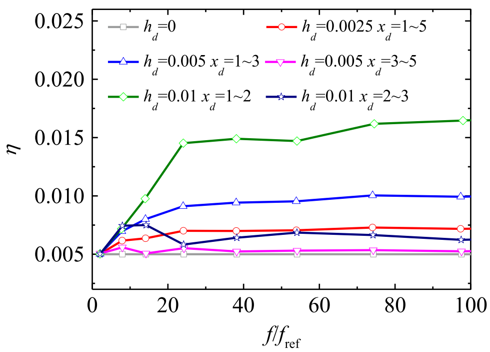

Fig. 8. Comparison of the system damping loss factors for different thicknesses and distributions of damping layers with constant mass. The length unit in the figure is cm.

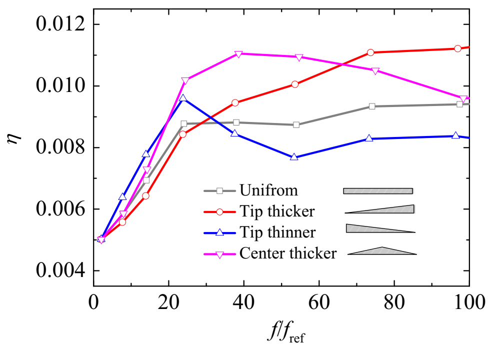

Fig. 9. Comparison of the system damping loss factors for different linear distributions of damping layers with constant mass while the uniform thickness damping layer corresponding to the condition of $h_d = 0.005$ cm and $x_d = 1$–2 cm.

the damping layers to achieve the most effective damping effect for a given application, for both free and forced vibration problems.

3.4. Effects of the full coupling

To evaluate the importance of the full coupling between the beam and the damping layers, Figs. 10 and 11 compare the system response with/without considering the mass and the stiffness of the damping layers, respectively. From Fig. 10(a), one can see that when the damping layer is uniformly applied over the whole ABH region with a thin thickness (only a half of the thickness of the ABH tip), the effect of the added mass by the damping layers is relatively small and negligible. When a thicker layer (double of the thickness of the ABH tip) only covers the tip region, however, the higher-order resonant frequencies are shifted to lower frequencies (the maximum reduction can be as large as 298 Hz in the present case) with the consideration of the mass of the damping layer, suggesting that, in this case, the added mass on the ABH tip area can be significant. This is understandable since ABH tip area dominates the vibration mode at these high frequencies as shown in

Fig. 3. However, both cases in Fig. 10 show the negligible effect of the damping layer mass on the overall vibration level of the structure. When considering the stiffness of the damping layers, for the same reason, the high order resonant peaks shift to high frequencies, more noticeably in Fig. 11(b). Meanwhile, a reduction in the mean quadratic velocity can also be observed in both cases, more noticeable for the tickers layer in Fig. 11(b).

3.5. *Effects of damping loss factor of damping layers*

When the damping loss factor of damping layers in the above numerical calculation is 0.3, the maximum reduced mean quadratic velocities of the uniform beam part can be as large as 11.3 dB compared with the bare beam without damping layers as demonstrated in Fig. 7. In practice, the damping loss factor of damping layers can be even larger for some polymers, especially when the material operates in its glass transition region [28]. Fig. 12 presents the reduced amplitude of mean quadratic velocities of the uniform beam part compared with bare beam for three typical damping loss factors for the first six resonant frequencies. The larger the damping loss factor is, the more the vibration level will be reduced as expected. The reduced mean quadratic velocities of the uniform part for larger damping loss factors at higher resonant frequencies can be appreciable (up to 14 dB in the best case).Therefore, significant damping effect can be achieved by making use of the ABH feature by properly choosing parameters and distribution of the damping layers.

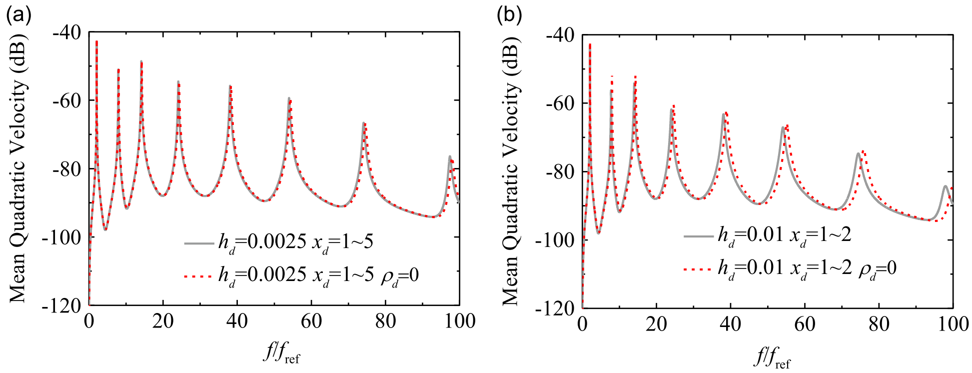

Fig. 10. The effect of the mass of damping layers on the mean quadratic velocity of the damping layers covered region for (a) thinner thickness and (b) thinker thickness compared with the thickness of beam tip.

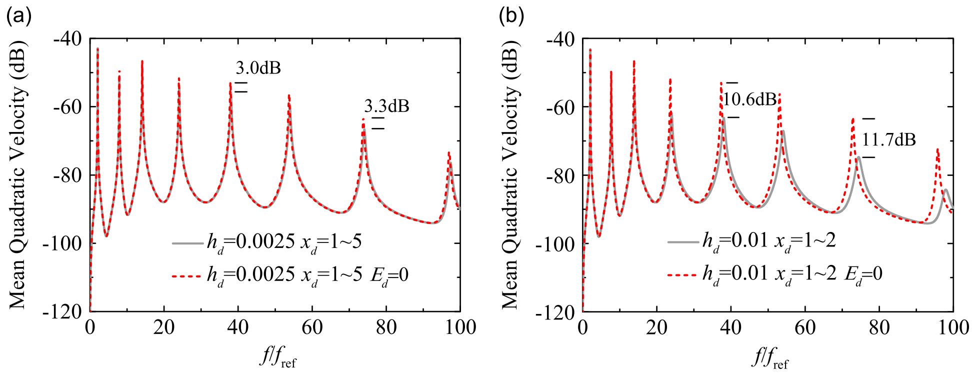

Fig. 11. The effect of the stiffness of damping layers on the mean quadratic velocity of the damping layers covered region for (a) thinner thickness and (b) thinker thickness compared with the thickness of beam tip.

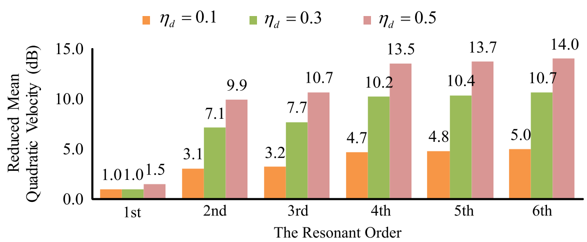

Fig. 12. Mean quadratic velocity reduction using damping layers with different damping loss factors (h_d=0.01 cm, x_d=1–5 cm).

4. Experimental validation

Experiments were conducted to further validate the accuracy of the present semi-analytical model. The test sample is illustrated in Fig. 13. The beam is made of steel with a mass density of 7794 kg/m^3 and Young modulus of 200 Gpa. The ABH portion parameters of the beam are: $\varepsilon = 0.00125$ cm^{-1} and $m = 2$. Other parameters are: $x_0 = 4$ cm, $x_{b1} = 16$ cm, $x_{b2} = 32$ cm. The whole beam has a uniform width of 1 cm. The beam was suspended by two thin strings to achieve free boundary conditions, thus eliminating the difficulty in realizing a clamped boundary due to the large stiffness of the beam. The beam was excited using an electromagnetic shaker at $x_f = 26$ cm, with the force measured through a force transducer (B&K 8200) and amplified by a charge amplifier (B&K 2635). A Polytec scanning laser vibrometer (PSV) was used to generate a periodic chirp signal with frequency from 0 Hz to 12 kHz to feed the shaker via a power amplifier (B&K 2706) and to scan the whole beam for response measurement.

The predicted cross point mobilities ($\dot{w}(x_m)/f(x_f)$) by the present model are compared with the experimental results in Fig. 14. As can be seen, the predicted results agree well with experimental ones, in terms of both amplitude and peak locations, especially for the frequency range covered by the first eight natural modes with an error typically less than 2 percent in terms of natural frequencies. The increasing error in higher frequencies is likely due to the neglected shear and torsional effect in the model, caused by the deviation of the excited force from the enteral axis. Fig. 15 shows the predicted mean quadratic velocity of the uniform part and that of the ABH part respectively against the experimental results. Again, both sets of results are in good agreement, demonstrating the remarkable accuracy of the proposed model. The ratios of mean quadratic velocity of the ABH portion to the uniform beam portion were also found to be in very good agreement (not shown here), confirming the energy concentration phenomenon revealed by the simulation model.

5. Conclusions

In this paper, a semi-analytical model is established to analyze an Euler–Bernoulli beam with embedded ABH feature and its full coupling with the damping layers coated over its surface. By using Mexican hat wavelet functions to approximate the flexural displacement, the governing equations are obtained based on Lagrange's equation. Highly consistent with experimental results as well as the FEM results in terms of the resonant frequencies and mode shapes, especially when a

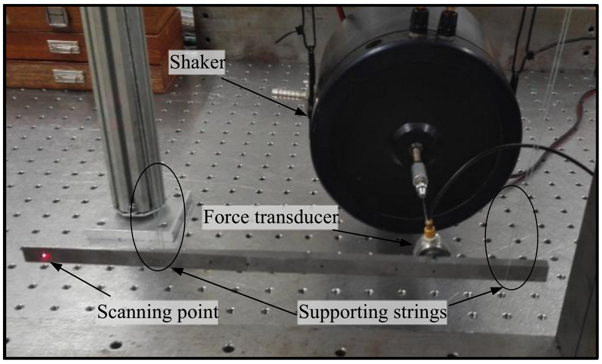

Fig. 13. Experimental set-up.

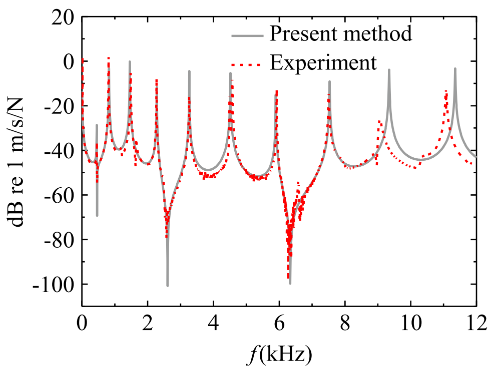

Fig. 14. Comparison of the predicted cross point mobility, $w(x_m = 5\ \text{cm})/f(x_f)$, against experimental measurements.

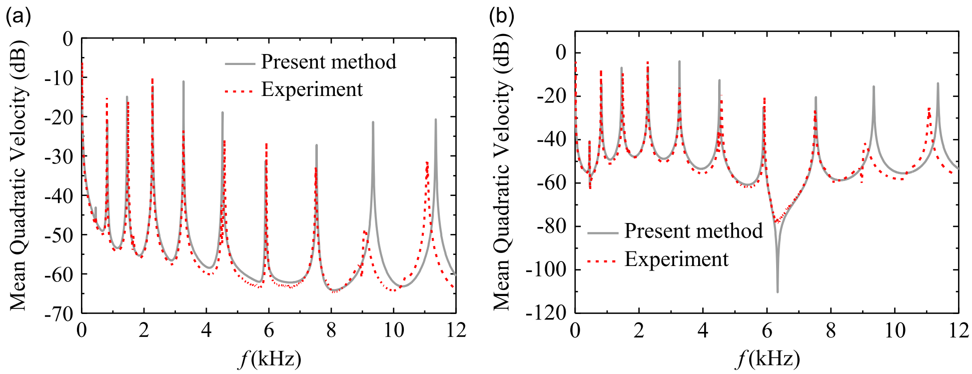

Fig. 15. Comparison of the prediction mean quadratic velocity of (a) the uniform beam portion, and (b) the ABH portion against experimental measurements.

truncation exists, numerical results demonstrate the validity and the suitability of the proposed wavelet-based model to characterize the wavelength fluctuation along the beam as a result of ABH effect.

The ABH effect enables a high energy density concentration in the vicinity of the ABH wedge tip, which is conducive to energy control and utilization within a confined area. However the truncation will weaken the ABH effect. Covering the ABH part with damping layers can compensate for the adverse effect of truncation and thus reduce the mean quadratic velocity of the uniform portion of the beam at high frequencies. Damping layers are preferable to be applied near the wedge tip as frequency increases. For a given problem, optimization through the proposed model is possible to find the exact damping layer configuration to achieve the maximum damping effect. Numerical results also indicate that the stiffness of the damping layers plays a more important role than the mass does, which should be apprehended in the model; while the effect of the added mass also needs particular attention when the thickness of damping layers is considerable to that of the ABH wedge around the tip area. As a general rule, the full coupling between the add-on elements such as the damping layers and the host structure is important to consider, which shows the importance of a fully coupled model.

As a final remark, the proposed model provides an efficient way to study the ABH feature and the effect of damping layers using a more realistic ABH-featured beam. The model is based on global expansion approach instead of meshing used in FEM, thus facilitating more flexible structural analyses and eventually system optimization at a later stage. Furthermore, due to its modular and energy-based nature, the proposed framework offers a general platform for further including other control or energy harvesting elements into the model to guide the design of ABH structures for various applications.

Acknowledgements

The authors would like to thank the Research Grant Council of the Hong Kong SAR (PolyU 152009/15E and PolyU 152026/14E), National Natural Science Foundation of China (No. 11532006) and the NUAA State Key Laboratory Program under Grants (MCMS-0514K01 and MCMS-0516K02) for financial support.

Appendix A. Formulas for M, K, and F

$$\mathbf{M}_{jiks} = \mathbf{M}_{jiks}^{\text{beam\_Uni}} + \mathbf{M}_{jiks}^{\text{beam\_ABH}} + \mathbf{M}_{jiks}^{damp}$$
$$(j, i = 0, 1, 2, \ldots, m, \quad k = -4+m-j+p(x_0 2^j): g(x_{b2} 2^j)+4-m+j, \quad s = -4+m-i+p(x_0 2^i): g(x_{b2} 2^i)+4-m+i)$$

$$\mathbf{M}_{jiks}^{\text{beam\_Uni}} = 2\rho_b h_b \int_{x_{b1}}^{x_{b2}} \varphi_{j,k}(x)\varphi_{i,s}(x)dx$$

$$\mathbf{M}_{jiks}^{\text{beam\_ABH}} = 2\epsilon\rho_b \int_{x_0}^{x_{b1}} \varphi_{j,k}(x)\varphi_{i,s}(x)x^m dx$$

$$\mathbf{M}_{jiks}^{\text{damp}} = 2\rho_d \int_{x_{d1}}^{x_{d2}} \varphi_{j,k}(x)\varphi_{i,s}(x)h_d(x)dx$$

$$\mathbf{K}_{jiks} = \mathbf{K}_{jiks}^{\text{beam\_Uni}} + \mathbf{K}_{jiks}^{\text{beam\_ABH}} + \mathbf{K}_{jiks}^{\text{damp}} + \mathbf{K}_{jiks}^{\text{edge}}$$
$$(j, i = 0, 1, 2, \ldots, m, \quad k = -4+m-j+p(x_0 2^j): g(x_{b2} 2^j)+4-m+j, \quad s = -4+m-i+p(x_0 2^i): g(x_{b2} 2^i)+4-m+i)$$

$$\mathbf{K}_{jiks}^{\text{beam\_Uni}} = \frac{2E_b {h_b}^3}{3} \int_{x_{b1}}^{x_{b2}} \frac{\partial^2 \varphi_{j,k}(x)}{\partial x^2} \frac{\partial^2 \varphi_{i,s}(x)}{\partial x^2} dx$$

$$\mathbf{K}_{jiks}^{\text{beam\_ABH}} = \frac{2E_b \epsilon^3}{3} \int_{x_0}^{x_{b1}} \frac{\partial^2 \varphi_{j,k}(x)}{\partial x^2} \frac{\partial^2 \varphi_{i,s}(x)}{\partial x^2} x^{3m} dx$$

$$\mathbf{K}_{jiks}^{\text{damp}} = \frac{2E_d}{3} \int_{x_{d1}}^{x_{d2}} \frac{\partial^2 \varphi_{j,k}(x)}{\partial x^2} \frac{\partial^2 \varphi_{i,s}(x)}{\partial x^2} \left(3\epsilon^2 x^{2m} h_d(x) + 3\epsilon x^m {h_d}^2(x) + {h_d}^3(x)\right) dx$$

$$\mathbf{K}_{jiks}^{\text{edge}} = k\varphi_{j,k}(x_{b2})\varphi_{i,s}(x_{b2}) + q \frac{\partial \varphi_{j,k}(x)}{\partial x}\Big|_{x = x_{b2}} \frac{\partial \varphi_{i,s}(x)}{\partial x}\Big|_{x = x_{b2}}$$

$$\mathbf{F}_{j,k} = \mathbf{F}\varphi_{j,k}(x_f)$$

References

[1] D. Ross, E.E. Kerwin, E.M. Ungar, *Damping of plate flexural vibrations by means of viscoelastic laminae, Structural Damping*, Pergamon Press, Oxford, 1960, 49–87.
[2] C. Vemula, A.N. Norris, Attenuation of waves in plates and bars using a graded impedance interface at edges, *Journal of Sound and Vibration* 196 (1996) 107–127.
[3] M.A. Mironov, Propagation of a flexural wave in a plate whose thickness decreases smoothly to zero in a finite interval, *Soviet Physics: Acoustics* 34 (3) (1988) 318–319.
[4] V.V. Krylov, A.L. Shuvalov, Propagation of localised flexural vibrations along plate edges described by a power law, *Proceedings of the Institute of Acoustics* 22 (2) (2000) 263–270.
[5] V.V. Krylov, Localised acoustic modes of a quadratically shaped solid wedge, *Moscow University Physics Bulletin* 45 (6) (1990) 65–69.
[6] V.V. Krylov, F.J.B.S. Tilman, Acoustic 'black holes' for flexural waves as effective vibration dampers, *Journal of Sound and Vibration* 274 (2004) 605–619.
[7] V.V. Krylov, New type of vibraion dampers utilizing the effect of acoustic black holes, *Acta Acustica United with Acustica* 90 (5) (2004) 830–837.
[8] D.J. O'Boy, V.V. Krylov, Damping of flexural vibrations in circular plates with tapered central holes, *Journal of Sound and Vibration* 330 (2011) 2220–2236.
[9] D.J. O'Boy, E.P. Bowyer, V.V. Krylov, Point mobility of a cylindrical plate incorporating a tapered hole of power-law profile, *Journal of the Acoustical Society of America* 129 (6) (2011) 3475–3482.
[10] E.P. Bowyer, D.J. O'Boy, V.V. Krylov, Damping of flexural vibrations in plates containing ensembles of tapered indentations of power-law profile, *Proceeding of Meetings on Acoustics* 18 (2013) 030003.
[11] E.P. Bowyer, V.V. Krylov, Sound radiation of rectangular plates containing tapered indentations of power-law profile, *Proceeding of Meetings on Acoustics* 18 (2013) 030002.
[12] S.C. Conlon, J.B. Fahnline, Numerical analysis of the vibroacoustic properties of plates with embedded grids of acoustic black holes, *Journal of the Acoustical Society of America* 137 (1) (2015) 447–457.
[13] L.X. Zhao, S.C. Conlon, F. Semperlotti, Broadband energy harvesting using acoustic black hole structural tailoring, *Smart Materials and Structures* 23 (2014) 065021.
[14] V.V. Krylov, Geometrical-acoustics approach to the description of localized vibrational modes of an elastic solid wedge, *Soviet Physics - Technical Physics* 35 (2) (1990) 137–140.
[15] P.A. Feurtado, S.C. Conlon, A normalized wave number variation parameter for acoustic black hole design, *JASA Express Letters* 136 (2) (2014) 148–152.
[16] V.B. Georgiev, J. Cuenca, F. Gautier, L. Simon, Vibration reduction of beams and plates using acoustic black hole effect, Inter noise, Lisbon, Portugal, June 13-16, 2010.
[17] V.B. Georgiev, J. Cuenca, F. Gautier, L. Simon, V.V. Krylov, Damping of structural vibrations in beams and elliptical plates using the acoustic black hole effect, *Journal of Sound and Vibration* 330 (2011) 2497–2508.
[18] E.P. Bowyer, D.J. O'Boy, V.V. Krylov, J.L. Horner, Effect of geometrical and material imperfections on damping flexural vibrations in plates with attached wedges of power law profile, *Applied Acoustics* 73 (2012) 514–523.
[19] L. Cheng, R. Lapointe, Vibration attenuation of panel structures by optically shaped viscoelastic coating with added weight considerations, *Thin-Walled Structures* 21 (1995) 307–326.
[20] L. Cheng, Vibroacoustic modeling of mechanically coupled structures: artificial spring technique applied to light and heavy medium, *Shock and Vibration* 3 (3) (1996) 193–200.
[21] C.D. Bailey, Direct analytical solutions to non-uniform beam problems, *Journal of Sound and Vibration* 56 (4) (1978) 501–507.
[22] S. Abrate, Vibration of non-uniform rods and beams, *Journal of Sound and Vibration* 185 (4) (1995) 703–716.
[23] H. Kobayashi, K. Sonoda, Vibration and buckling of tapered rectangular plates with two opposite edges simply supported and the other two edges elastically restrained against rotation, *Journal of Sound and Vibration* 146 (1991) 323–337.
[24] S.F. NG, Y. Araar, Free vibration and buckling analysis of clamped rectangular plates of variable thickness by the Galerkin method, *Journal of Sound and Vibration* 135 (1989) 263–274.
[25] I. Daubechies, Ten lectures on wavelets, CBM-NSF conference series in applied mathematics, SIAM ED, Philadelphia, 1992.
[26] T. Hou, H. Qin, Continuous and discrete Mexican hat wavelet transform on manifolds, *Graphical Models* 74 (2012) 221–232.
[27] S.S. Rao, F.F. Yap, *Mechanical Vibrations*, Addison Wesley, Massachusetts, 1995.
[28] R.D. Corsaro, L.H. Sperling, *Sound and Vibration Damping with Polymers*, American Chemical Society, Washington, 1990.